ACS APPLIED MATERIALS & INTERFACES

Research Article

www.acsami.org

Wet Nanoindentation of the Solid Electrolyte Interphase on Thin Film Si Electrodes

Volodymyr Kuznetsov,[†] Arndt-Hendrik Zinn,[‡] Giorgia Zampardi,[†,§] Sara Borhani-Haghighi,[‡] Fabio La Mantia,[§,⊥] Alfred Ludwig,[‡,∥] Wolfgang Schuhmann,[*,†,∥] and Edgar Ventosa[*,†]

[†]Analytical Chemistry - Center for Electrochemical Sciences (CES), Ruhr-University Bochum, Universitätsstraße 150, 44780 Bochum, Germany

[‡]Institute for Materials, Ruhr-University Bochum, Universitätsstraße 150, 44801 Bochum, Germany

[§]Semiconductor & Energy Conversion − Center for Electrochemical Sciences (CES), Ruhr-Universität Bochum, 44780 Bochum, Germany

[∥]Materials Research Department, Ruhr-Universität Bochum, Universitätsstr.150, 44780 Bochum, Germany

[⊥]Energiespeicher- und Energiewandlersysteme, Universität Bremen, Wiener Str. 12, 28359 Bremen, Germany

ABSTRACT: The solid electrolyte interphase (SEI) film formed at the surface of negative electrodes strongly affects the performance of a Li-ion battery. The mechanical properties of the SEI are of special importance for Si electrodes due to the large volumetric changes of Si upon (de)insertion of Li ions. This manuscript reports the careful determination of the Young's modulus of the SEI formed on a sputtered Si electrode using wet atomic force microscopy (AFM)-nanoindentation. Several key parameters in the determination of the Young's modulus are considered and discussed, e.g., wetness and roughness−thickness ratio of the film and the shape of a nanoindenter. The values of the Young's modulus were determined to be 0.5−10 MPa under the investigated conditions which are in the lower range of those previously reported, i.e., 1 MPa to 10 GPa, pointing out the importance of the conditions of its determination. After multiple electrochemical cycles, the polymeric deposits formed on the surface of the SEI are revealed, by force-volume mapping in liquid using colloidal probes, to extend up to 300 nm into bulk solution.

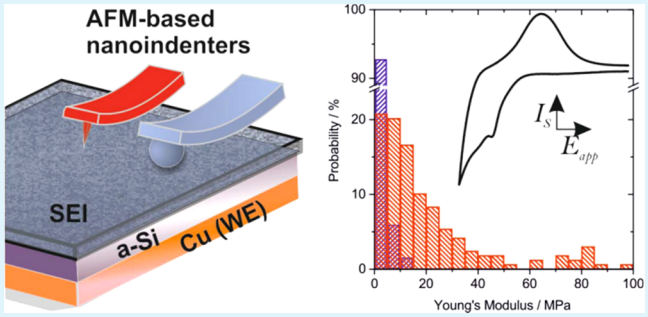

KEYWORDS: *Li-ion battery, silicon electrode, solid electrolyte interphase (SEI), atomic force microscopy (AFM), mechanical properties, Young's modulus, nanoindentation, colloidal probe force microscopy*

1. INTRODUCTION

Li-ion batteries (LIBs) possess the highest energy densities among all energy storage technologies, which make them the power source of choice for portable electronic devices and automotive applications. Although the energy density of state-of-art batteries is sufficient for hybrid electric vehicles (HEVs), the performance of currently available LIBs falls short for plug-in hybrid electric vehicles (PHEVs) and pure electric vehicles (EV).[1] Increasing the energy density by using abundance and low-cost active material with larger Li storage capacity is seen as a prerequisite to pave the way toward large-scale deployment of LIBs in PHEVs and EVs.

Si is the most promising negative electrode material since it is the second most abundant element on earth and the second largest Li storage material (4200 mA h g^{-1}), only after metallic Li.[2,3] In addition, Si has a very catholic (de)insertion potential of 0.1−0.4 V vs Li/Li^+, which results in large battery cell voltage. The cathodic Li (de)insertion potential of Si requires operating outside the electrochemical stability window of carbonate-based electrolyte solutions. As is known for graphite electrodes, the reductive decomposition of the electrolyte may lead to the formation of a protective film referred to as solid electrolyte interphase (SEI). Fortunately, the SEI is permeable for Li-ions, but it is an electrical insulator, which avoids further electrochemical decomposition of the electrolyte. In graphite electrodes, the SEI formation occurs over the first few cycles, predominantly during the first one. However, this is not the case for Si electrodes, and electrolyte decomposition occurs over many cycles due to the large volumetric changes of Si upon Li-ion (de)insertion. The continuous decomposition of the electrolyte lowers the Coulombic efficiency, depletes the concentration of Li-ions, and increases the internal resistance by thickening of the SEI film. In addition, the volumetric changes of Si not only affect the electrode−electrolyte interface but also are the source of most of the limiting issues of the material itself. The mechanical stress caused by the volumetric

Received: July 23, 2015
Accepted: September 29, 2015
Published: September 29, 2015

DOI: 10.1021/acsami.5b06700
ACS Appl. Mater. Interfaces 2015, 7, 23554−23563

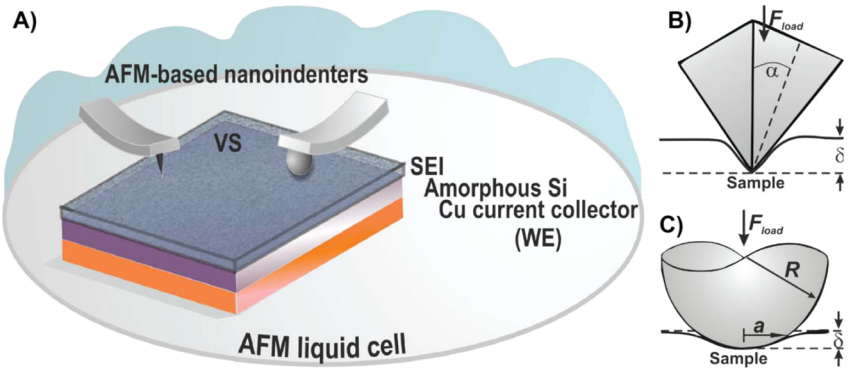

Figure 1. (A) Schematic representation of the experimental setup to measure mechanical properties of the SEI on a Si electrode (50 nm) by indentation with a sharp AFM tip or by a spherical colloidal probe. Sketch of the indentation (B) by a four-sided pyramid and (C) for a spherical indenter.

changes of Si upon cycling leads to fraction and pulverization of Si electrodes. The electrically insulating SEI is then responsible for disconnecting the fragmented Si from the current collector, which leads to the fading of the reversible specific charge upon cycling. Therefore, it is imperative to understand the mechanism and properties of the SEI to enhance the performance of Si electrode.

Among techniques employed to characterize the SEI, atomic force microscopy (AFM) has been widely used to evaluate its morphology as well as its thickness.[4−6] In addition, AFM-based methods can provide information about the mechanical properties of the SEI, such as the Young's modulus.[7−11] However, probing thin films by indentation is challenging, and special attention must be paid to address several important aspects, e.g., morphology or surface properties such as roughness and adhesiveness to minimize errors and obtain reliable results.[12,13]

In the present work, we report the determination of the Young's modulus of the SEI formed on Si sputtered electrodes by wet AFM-nanoindentation. In order to minimize the systematic error, we evaluated the morphology evolution of the SEI films upon electrochemical cycling and compared values obtained by using two types of nanoindenters, i.e., a pyramidal and a spherical one. In addition, we carried out the nanoindentation in liquid to keep the film wet to mimic the operation conditions.

2. EXPERIMENTAL SECTION

2.1. Materials. All solvents and salts used for this work were anhydrous (dry). Ethylene carbonate (EC) (99%, Sigma-Aldrich), propylene carbonate (PC) (99.7%, Sigma-Aldrich), $LiClO_4$ (battery grade, ≥99.99%, Sigma-Aldrich), and $LiPF_6$ (battery grade, ≥99.99%, Sigma-Aldrich) were used as received.

2.2. Electrode Preparation. Silicon (Si) undergoes severe volumetric expansion upon lithium insertion that is accompanied by crack formation.[14] Because a flat surface is required for subsequent AFM analysis, the crack formation is mitigated by the use of a 50 nm thin film that did not show cracking in earlier studies.[15] For electrical connection, a 200 nm thick Cu (99,99%; AJA International) current collector is sputter deposited on 150 μm thermally grown SiO_2 on a Si wafer (4 in. diameter and 525 μm thick, Sieger Wafer), followed by amorphous Si deposition (99.999%; Sindlhauser). Layers of Ti (10 nm, 99.97%; K.L. Lesker) as an adhesion-promoter were deposited between the wafer and the Cu layer and between the Cu layer and Si. All depositions were executed in Ar (99.999%, partial pressure 0.66 Pa, flow 20 sccm with a gas filter in place) at 150 W DC power, except for the amorphous Si, which was deposited by radio frequency (RF) magnetron sputtering at 150 W. To prevent the oxidation at all stages of fabrication including the subsequent handling, the sputter chamber is located in an Ar-filled glovebox. To prevent the formation of native SiO_2, samples were transferred in sealed containers without air exposure. In an earlier study, Si thin film deposited under similar conditions was found by XRD analysis to be amorphous with crystalline intermetallic phases forming at the layer interface.[16]

2.3. SEI Formation. Electrochemical and AFM experiments were carried out inside a glovebox (Jacomex, France) filled with Ar in order to exclude any trace of O_2 and H_2O (below 3 ppm). The homemade three-electrode electrochemical cell (made of PEEK) had the sputtered sample as working electrode (WE), geometric area of ca. 0.196 cm^2, a large cylindrical Ti mesh (Alpha Aesar) covered with carbon nanotubes as counter electrode (CE), and a Li/Li^+ reference electrode in 1 M $LiClO_4$ in EC:PC (1:1 wt %) separated from the electrolyte by a frit.[17] Both the counter electrode and the reference electrode are immersed in the electrolyte from the top of the cell. A solution consisting of 1 M $LiPF_6$ in PC was used as electrolyte solutions. The formation and evolution of the SEI was controlled by cyclic voltammetry (lithiation−delithiation cycles) performed with a μ-Autolab potentiostat, type III, positioned outside the glovebox. After the electrochemical formation of the SEI, the CE and RE were removed and the AFM head was immediately positioned and approached to the surface while keeping the liquid for wet conditions. A possible in situ experiment was discarded because it would introduce a drastic distortion of the current lines in the cell, which leads to inhomogeneous current density distribution and inhomogeneous growth of the SEI film.

2.4. AFM Imaging and Indentation Measurements. A Nanowizard 2 AFM (JPK Instruments) was used for imaging and force measurements. Data analysis was carried out with the JPK software package (JPK Data Processing v. 4.2.53.) according to standard procedures.[13] Surface topography was characterized with commercial high-resolution Si cantilevers (Hi'Res19/Cr−Au, AppNano) by tapping mode in liquid. Sharp pyramidal AFM tips, referred to as S-AFM tips, and silica colloidal probes were used for AFM indentation, as schematically shown in Figure 1A. Robust spherical colloidal probes (CPs) were prepared according to a standard procedure as described elsewhere.[18] For this purpose, clean tipless AFM cantilevers (AIO-TL-10, BudgetSensors) with stiffness of 0.29−3.1 N m^{-1} were calibrated by the thermal noise method.[19] Afterward, spherical silica particles (⌀ = 6.8 μm, surface roughness below 2.1 nm rms, Bangs Laboratories, IN) were attached to the cantilevers by a mixture of UV-curable glue (Optical adhesive 63, Norland Products) and dried SiO_2 nanoparticles (Ludox AM, SigmaAldrich) and subsequently exposed to UV radiation for at least 1 h. The precured CPs were further treated at high temperature (1250 °C, 2 h) to allow the sintering of particles to cantilevers. Clean AFM cantilevers with pyramidal tips, stiffness of 0.19−40 N m^{-1} (CSC17 and NSC15, AppNano), were calibrated by the thermal noise method.[19]

The performance of CPs and S-AFM tips was evaluated with block copolymers ESTANE ETE75DT3 NAT022 (T_g = 55 °C; bulk E = 85

DOI: 10.1021/acsami.5b06700
ACS Appl. Mater. Interfaces 2015, 7, 23554−23563

MPa at r.t.) and ESTANE 58300 NAT035 (T_g = −27 °C; bulk E = 19 MPa at r.t.) in argon atmosphere.[20] The local values of E, determined by nanoindentation (indentation depth below 10 nm), comply within 30% of the bulk values. Before and after every nanoindentation measurement in the electrochemical cell, the sensitivity of CPs and S-AFM tips was determined in liquid (PC) by hard-wall indentation against 150 μm thermally grown SiO_2 on a Si wafer. The typical indentation speed was 800 nm s^{-1}. Upon lowering the speed below ca. 500 nm s^{-1}, the mechanical noise becomes tremendous, while after increasing the rate above 1400 nm s^{-1}, the liquid drag effect starts to play a role. Within this given interval, however, no variation of apparent elasticity was observed. Stiffer cantilevers were applied on harder materials to fulfill the common sensitivity criteria.[21] To collect representative statistics, we used force-volume data acquisition (micromapping) with 8 × 8 points over a 50 μm × 50 μm array. Force−indentation curves were excluded from analysis if the noise in the data did not allow consistent fitting by the corresponding model. Sources of systematic errors are discussed in the Theoretical Basis section.

3. THEORETICAL BASIS

Both standard AFM tips (S-AFM, Figure 1B) and spherical colloidal probes (CPs, Figure 1C) may be used to assess the mechanical properties of organic films. However, for thin film thickness below 100 nm, these indenters have high methodological inaccuracy independent of the model used for the data analysis.[22,23] First, inadequately defined AFM tip geometry causes underestimation of the contact area, especially for indentation depths in the order of the assumed tip gyration radius (typically 5−10 nm).[12] Since by definition

$$E = \frac{\text{tensile stress}}{\text{tensile strain}} = \frac{F_{load} \cdot L}{A \cdot \Delta L} \quad (1)$$

where F_{load} is the applied force, which causes intrinsic linear film deformation $\Delta L/L$ over the contact area A. From eq 1, it is evident that, the larger the real area, the smaller is the deduced elasticity, while using a model-defined value of A with an experimentally measured F_{load} overrates the apparent elasticity E. Therefore, the elasticity of thin films measured with the S-AFM tip tends to be overestimated. Indeed, this is the case for the most widely used evaluation models of the Young's modulus such as Hertz, Sneddon, and JKR.[22] However, S-AFM tips allow unprecedentedly high local resolution of the mechanical properties, which helps to circumvent surface roughness effects. In contrast to sharp tips, the use of CPs with regularly shaped spherical indenter provides well-defined contact geometry. The CP averages the elastic response over a large area during the measurement. That increases the precision of elastic modulus evaluation since the bulk inhomogeneities of the film are masked, but it causes a systematical error if the surface roughness is considerable as compared to the indentation depth. Due to the surface roughness of a sample, a compliant contact between the indenter and the sample may not be achieved. Consequently, the real surface area A would be smaller than the apparent one, and the calculated elasticity E would be underestimated. Thus, the values of thin film elasticity are overestimated and underestimated when using S-AFM tips and CPs, respectively.

Hertz model and its numerous modifications are commonly adopted as standard models for analyzing the force−indentation curves in order to extract the Young's modulus.[13] The model variations for numerous simple indentation geometries differentiate by the effective radius of the contact region. Typically, it is assumed in the simplified formula that the stiffness of the AFM indenter is much higher than the one of the probed material. The assumption is valid for the indentation by silicon S-AFM tips and quartz CPs of soft SEI films. Precisely, the elasticity and Poisson ratio of Si vary in the range of 130−185 GPa and ν = 0.26−0.28, respectively, depending on crystallographic orientation, while the values for silicon oxide (fused quartz) are 72 GPa and 0.17.[13] On the other hand, the elasticity of the SEI, reported up to date, is in the range from 1 MPa to 10 GPa.[7−11] The Poisson ratio of the anisotropic SEI is likely to be between 0.5 and 0.25, which is typical for polymeric composite materials.[24] We used the modification of Bilodeau[25] for the four-sided pyramid indenter for the numerical fitting of the force−indentation data obtained with AFM tip

$$E = \frac{1}{0.7453}\frac{F_{load}(1-\nu^2)}{\delta^2 \tan(\alpha)}; \quad F_{load} = 0.7453\frac{E}{(1-\nu^2)}\delta^2 \tan(\alpha) \quad (2)$$

where E and ν are the Young's modulus and a Poisson ratio of the sample, respectively; δ and α are the indentation depth and the half cone angle (Figure 1B). The eq 2 differs from the Sneddon's conical indenter model by a small fixed factor of ca. 1.17. While the latter model assumes circular symmetry of the indenter, giving corresponding contact radius $a = 2\delta\tan(\alpha)/\pi$, Bilodeau provides an approximation for asymmetrical geometry of $a = 0.709\delta\tan\alpha$.[25]

We employed the classical parabolic indenter model for numerical fitting of the force−indentation data obtained with CPs:

$$E = \frac{3}{4}\frac{F_{load}(1-\nu^2)}{\delta^{3/2}\sqrt{R_{CP}}}; \quad F_{load} = \frac{E}{(1-\nu^2)}\frac{4\sqrt{R_{CP}}}{3}\delta^{3/2} \quad (3)$$

where R_{CP} is the radius of CP (Figure 1C) and the contact radius is given by $a = (2R_C\delta)^{1/2}$. The use of two indenter geometries in parallel, namely, pyramidal of S-AFM tips and spherical CPs, is expected to overlay their benefits and exclude the systematic inaccuracies from the final distribution of the thin film Young's modulus.

4. RESULTS AND DISCUSSION

To study the formation, evolution, and mechanical properties of SEI on amorphous Si, we employed cyclic voltammetry in a three-electrode cell and atomic force microscope (AFM), which could be placed in situ. The AFM was not installed in the cell during the electrochemical experiment, but a large counter electrode was integrated instead. This was a necessary measure to secure a homogeneous current density distribution at the surface of the Si working electrode. As soon as an electrochemical experiment was stopped, we installed the AFM head and acquired the corresponding data.

4.1. Electrochemical Formation and Morphological Characterization of the SEI. The electrochemical formation of the SEI was carried out by cyclic voltammetry. Figure 2 shows the first 10 cyclic voltammograms of amorphous silicon in 1 M $LiPF_6$ in PC at a scan rate of 0.5 mV s^{-1}. The scan starts at 1.5 V vs Li/Li^+ in the cathodic direction until the cutoff potential of 0.1 V is reached. During the first cycle, the formation of the SEI is manifested by an abrupt increase in current intensity during the cathodic scan at 0.5−0.3 V vs Li/Li^+, as typically observed for amorphous silicon in various electrolyte systems.[26,27] In subsequent cathodic cycles, the current intensity in the potential range of 0.5−0.3 V decreases significantly, which suggests that most of the SEI is formed

DOI: 10.1021/acsami.5b06700
ACS Appl. Mater. Interfaces 2015, 7, 23554−23563

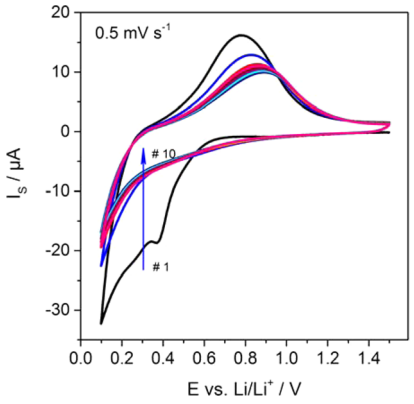

Figure 2. Cyclic voltammograms (first 10 cycles) of sputtered Si thin film electrode in 1 M $LiPF_6$ in PC within the potential range of 1.5–0.1 V vs Li/Li^+ at a scan rate of 0.5 mVs^{-1}.

during the first cathodic scan. During the anodic scan, a single peak is observed at about 0.8 V, which is attributed to the deinsertion of Li-ions from the Si electrode. The current intensity of the peak decreases and shifts toward more anodic potentials during the first 3 cycles. After 3 cycles, the electrochemical signal stabilizes and the subsequent cyclic voltammograms overlap. Partial fragmentation of the Si electrode is likely to be responsible for the changes in the anodic peak. In fact, a lower cutoff potential was intentionally set to 0.1 V to prevent severe fragmentation of the electrode, in comparison with the widely used lower cutoff potential of 0.05 or 0.01 V. This strategy has been employed in other studies to limit the volume expansion upon lithiation, minimizing the detrimental effects that large volumetric changes induce on the Si electrode.[28,29]

The topography of the surface of a Si electrode was evaluated in liquid before cycling and after 1, 3, and 10 cycles. Figure 3A shows the topography of an amorphous Si sample before cycling showing a relatively smooth surface considering the height scale of 30 nm. After the first cycle, the surface became smoother and more homogeneous (Figure 3B). This suggests homogeneous formation of the SEI film across the electrode, filling small pores and leading to the smoothening of the electrode surface. However, subsequent cycles led to roughening of the surface. To account for this effect, the *z*-color scale bar had to be changed from 30 to 100 nm. Figure 3C depicts the surface topography after 3 cycles. In addition to the roughening of the surface, weakly attached globular-like formations ("hill-like" according to Deng et al.[10]) were seen on the rough surface, which were approximately 50–200 nm in diameter. The globular-like formations were laterally movable on the surface as deduced from characteristic pseudonoise lines on the image, where the given topographical elements disappear abruptly. Similar changes in SEI topography during the first two cycles were observed before by Lucas et al., who investigated SEI formation on a Sn electrode by in situ AFM.[30] It should be noted that the resolution of our images (1 × 1 μm^2) is higher than that previously reported (typically 5^2, 8^2 and 10^2 μm^2).[4,30] The surface topography after 10 cycles (Figure 3D) reveals that the apparent surface roughness has decreased as compared to the third cycle, resulting in a rather homogeneous surface covered with globular-like structures with a size generally below 50 nm in diameter. Thus, the surface topography of Si electrodes undergoes drastic irreversible changes upon formation of the SEI during 10 (de)insertion cycles. The evolution of the surface topography upon cycling indicates the importance of the mechanical properties of the SEI to withstand the volumetric changes of Si electrodes.

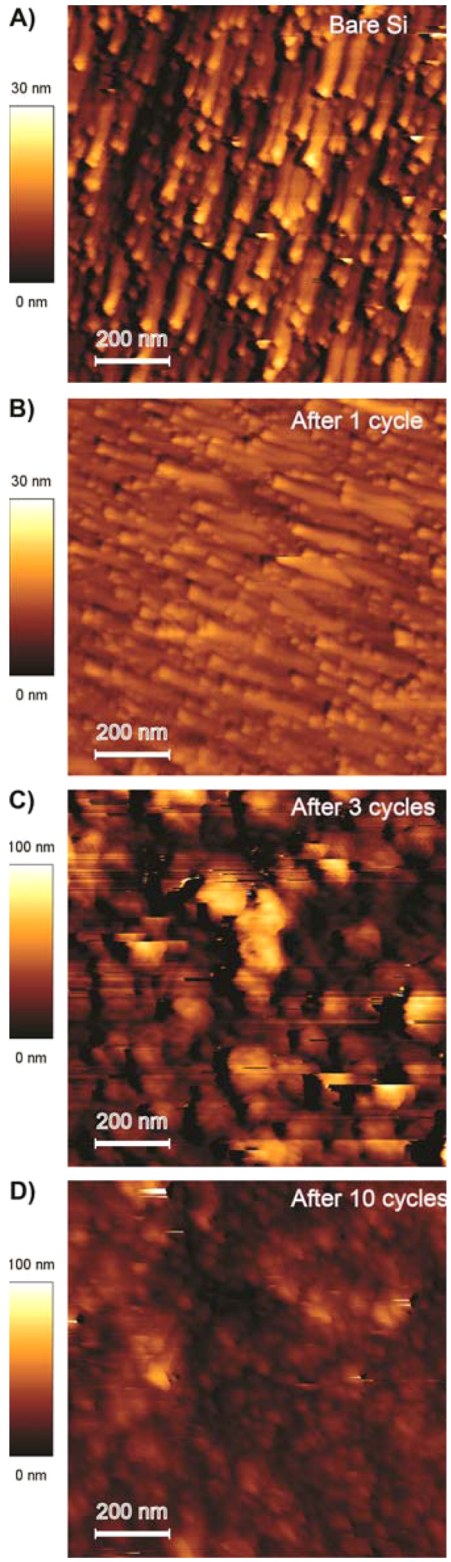

Figure 3. AFM topography of the surface of a Si electrode (A) before cyclic voltammetry and after (B) 1 cycle, (C) 3 cycles, and (D) 10 cycles. AFM images were acquired in tapping mode in liquid. Image size is 1 μm × 1 μm. Note that the height-scale changes: 30 and 100 nm for (A, B) and (C, D), respectively.

DOI: 10.1021/acsami.5b06700
ACS Appl. Mater. Interfaces 2015, 7, 23554–23563

The evolution of the surface topography can be quantitatively represented by surface roughness factors. The commonly used factors are the root-mean-square roughness R_{rms} (rms roughness) and the peak-to-peak roughness R_z, which represent the average of height deviations measured from the mean line and the absolute value between the highest and the lowest peaks within a given area, respectively. Table 1 summarizes the representative values of surface roughness factors obtained for a Si electrode at different cycling conditions. The formation of the SEI after the first cycles led to a decrease in R_{rms} from 5 nm (prior to cycling) to 2 nm (after the first cycle). This indicates that the cavities on the electrode are filled faster than the protruding parts of the electrode. The following two consecutive scans cause rms roughness to increase drastically up to R_{rms} of ca. 16 nm. Then, the roughness decreases slowly, reaching R_{rms} of 10 nm after 10 (de)insertion cycles. Qualitatively similar trends in roughness variation were observed for R_z.

Table 1. Evolution of the Surface Roughness on Si Electrodes Determined by AFM in Liquid[a]

condition	rms roughness R_{rms}, nm	peak-to-peak roughness R_z, nm
prior to cycling	5.1 ± 0.4	ca. 39
after 1 cycle	1.9 ± 0.1	ca. 12
after 3 cycles	16 ± 5.2	ca. 110
after 10 cycles	10 ± 3.3	ca. 80

[a]The evaluated area was 1 × 1 μm^2.

4.2. Mechanical Properties of the SEI. First of all, it should be noted that multiple parameters can influence the mechanical properties and thickness of SEI like composition of electrolyte solution, operating voltage, charging rate, temperature, etc. The values of mechanical properties reported in this work are valid for the investigated conditions.

In Section 3, we discussed several parameters that affect the uncertainty of the estimated value of the Young's modulus. Having a rough thin film may impede obtaining a reliable value. Indeed, the surface roughness together with the film thickness, which determines the indentation depth, defines the experimental error of indentation measurements. If roughness exceeded the indentation depth, random error would increase unsustainably. The relatively high surface roughness observed on Si electrodes after multiple cycles (Table 1) may compromise the determination of the mechanical properties of the SEI. Therefore, we initially attempted to assess whether or not the mechanical properties of the SEI after multiple cycles can be reliably determined. First, the thickness of the SEI (after

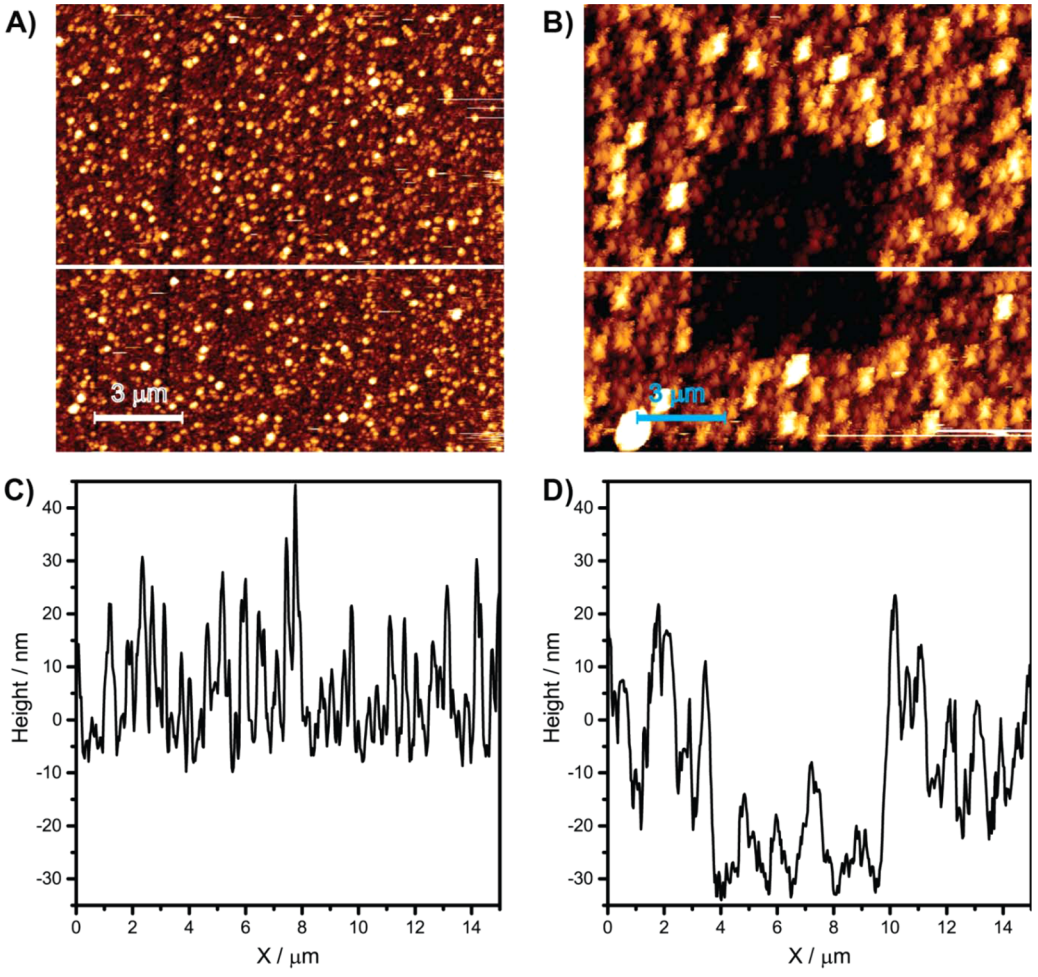

Figure 4. AFM topography of Si after 10 lithiation−delithiation cycles before (A) and after (B) the scratch test. *z*-scale is 60 nm for both images. The corresponding image cross sections are shown in (C) and (D). Scratching (5 × 5 μm^2) was performed in contact mode at a loading force of about 40 nN. The AFM tip was clearly damaged or contaminated during scratching causing tip convolution artifacts, which however does not affect the film thickness determination.

DOI: 10.1021/acsami.5b06700
ACS Appl. Mater. Interfaces 2015, 7, 23554−23563

10 cycles) was estimated following a previously reported method based on scratching away a part of the film and measuring the gap. Shortly, the SEI was scratched in a 7 × 7 μm^2 area at a loading force of ca. 50 nN, following a 15 × 15 μm^2 area imaging in tapping mode (Figure 4A). The reference experiment for scratching the bare Si surface at 50 nN indicates that the surface could not be damaged under such conditions. Due to the tip wear during the scratching in contact mode, the subsequent AFM image (Figure 4B) is affected by tip convolution artifacts. The latter, however, does not prevent the determination of the SEI thickness from corresponding cross sections (Figure 4C,D). The thickness of the SEI after 10 cycles was estimated to be in the order of 25−30 nm. With a typical indentation depth in the order of 10−20% of a thin film, the indentation depth is estimated at 3−6 nm. The rms roughness of this sample (10 nm after 10 cycles or 16 nm after 3 cycles) is higher than the expected indentation depth (3−6 nm), which impedes acquisition of force−indentation curves with realistic contact point estimation. Consequently, the reliable determination of the Young's modulus is not possible for the SEI after multiple cycles. Nanoindentation can yield valuable force curves only before the first rupture of the SEI, i.e., immediately after the first (de)insertion cycle.

Although reliable values of the Young's modulus cannot be derived for the investigated silicon electrodes after multiple cycles due to the rough surfaces, the nature of the weakly attached globular-like formations was investigated by force-volume mapping. A single point of such a mapping includes an approach of the AFM cantilever toward the surface until the specified loading force is applied to the surface followed by subsequent retraction. Since the globular-like formations appear to be moveable and weakly attached to the surface, spherical CPs with relatively large contact area were employed. Figure 5A shows an approach and retraction curve of a spherical CP to the SEI formed after the first (de)insertion cycle. The first contact with a solid substance is associated with an apparent increase of the repulsion force. This first contact is further addressed as zero indentation depth (X = 0 nm). The hysteresis in approach and retraction curves in Figure 5A could have been caused by a plastic deformation of the SEI. The spherical CPs do not penetrate through the film but compress it. As a consequence, strong repulsion forces are observed for a few nanometers after contact with the SEI. However, force curves acquired after the 3rd and 10th cycles appear different as shown in Figure 5B,C, respectively. In both cases, the profile shows a weak repulsion after reaching the contact point upon approach. The distance of weak repulsive interactions (so-called steric repulsion) increases with the number of cycles applied to the Si electrode, namely, ca. up to 100 nm and up to 300 nm for 3 and 10 cycles, respectively. We estimated from the scratching test that the thickness of the SEI after 10 cycles was about 25 to 30 nm. This suggests that the polymeric formations that accounts for at least 250 nm are weakly attached to the surface. Values of the Young's modulus determined from fitting this part of the curves (the first 250 nm) are in the order of hundreds of Pa, which are several orders of magnitude below the expected values for the SEI. We interpret this behavior as an interaction with the polymeric residues on the SEI surface,[31] which are likely to emerge from debris formed upon the periodic rupture of the SEI upon cycling.

The origin of the SEI degradation lies in the structural and morphological changes of the Si electrode upon cycling, which leads to (1) specific charge losses due to the SEI formation and

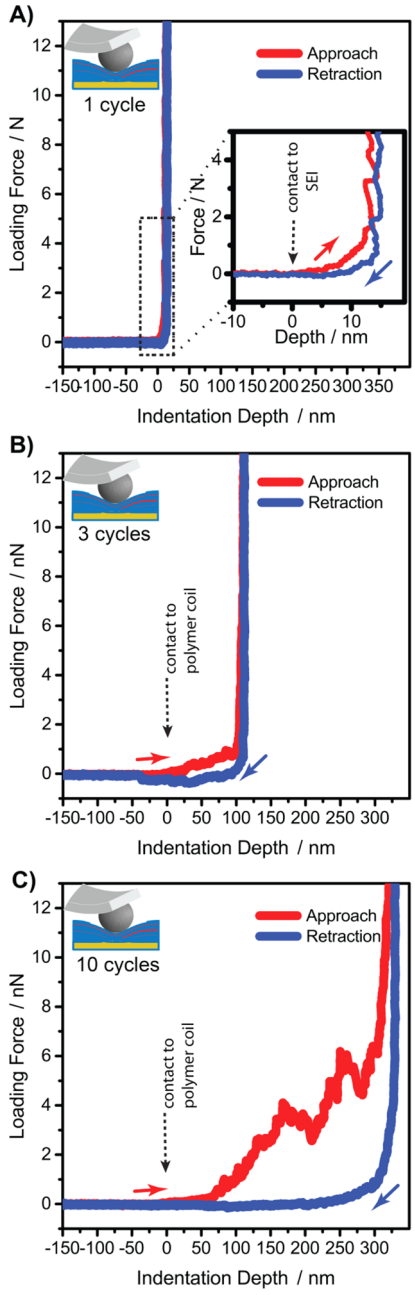

Figure 5. Typical force−indentation curves measured by means of a spherical colloidal probe on the SEI formed after the 1st cycle (A), the 3rd cycle (B), and the 10th cycle (C). Both approach (red) and retraction (blue) curves are shown.

renewal; (2) an increase in ohmic resistance; and (3) irreversible lithium accumulation in the SEI.[32] Since the SEI can be considered as a composite polymeric film, its elastic and adhesive behavior are essential parameters.[33,34] When the elasticity of the SEI is not sufficient to adapt reversibly to the electrode deformation, delamination or detachment of the SEI or its rupture is expected. Our results suggest a periodic rupture of the SEI upon cycling with subsequent formation of debris observed directly and indirectly as shown in Figures 3 and 4. Moreover, the detached globular-like formations on the SEI behave mechanically like a polymer, which supports earlier observations of Deng et al.[10] for glassy carbon and of Liu et al.[11] for Si nanowires and Cu film. It should be noted that the lateral strains are considerably higher on the convex surface of

DOI: 10.1021/acsami.5b06700
ACS Appl. Mater. Interfaces 2015, 7, 23554−23563

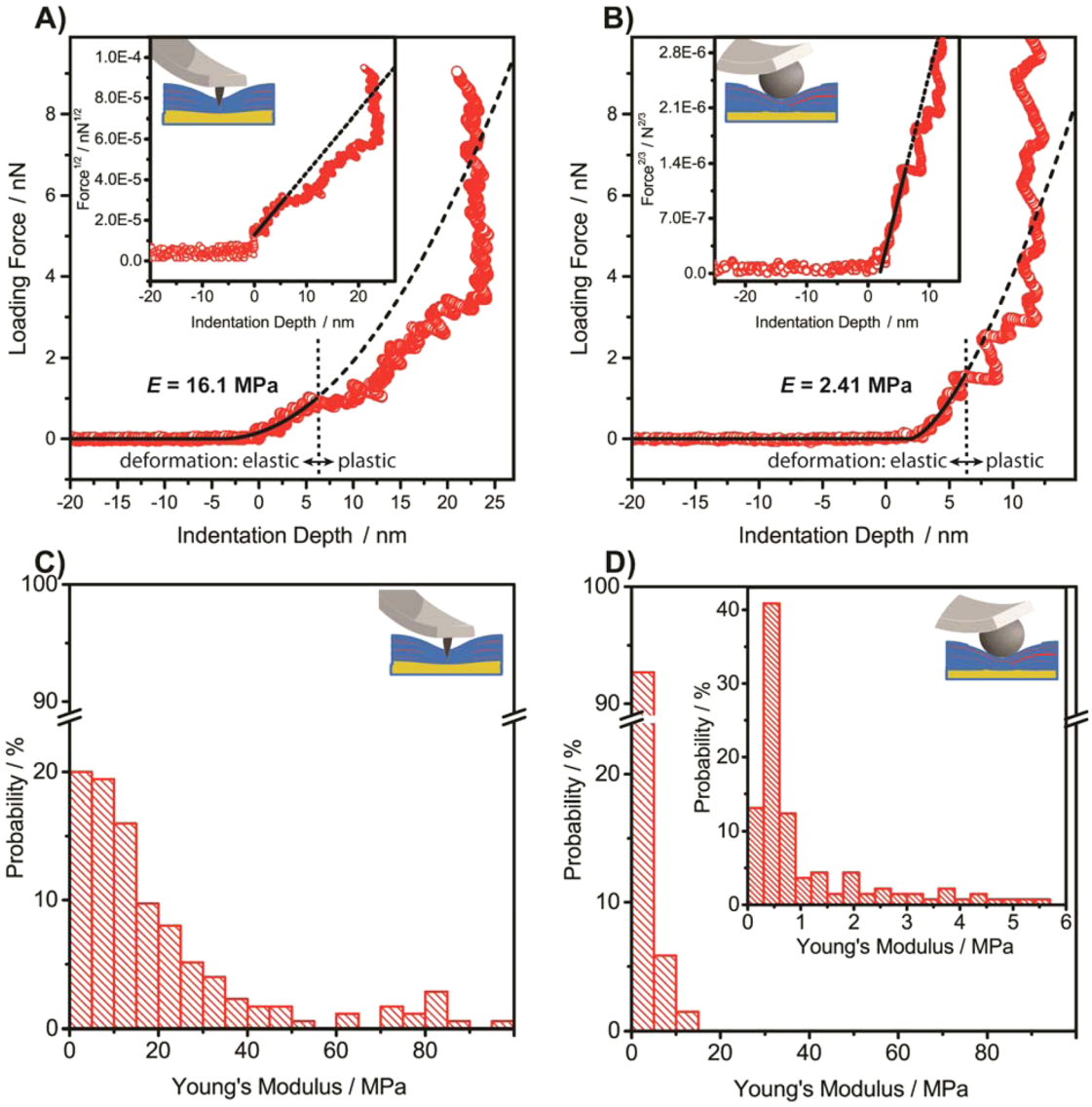

Figure 6. Force−indentation curves obtained (A) with a pyramidal S-AFM tip (cone angle ca. 35°) and (B) a spherical CP (⌀ ca. 6.8 μm). Only the part with elastic deformation was fitted (full line), while the dashed line shows extrapolation. The slopes of the indentation curves in semilogarithmic representation confirm the corresponding indenter geometry as shown in the insets.[38] The related distribution of the apparent Young's modulus of the SEI as determined by (C) S-AFM tip (count number N = 175) and by (D) CP (count number N = 137). The SEI obtained after the 1st lithiation−delithiation cycle was used for the experiments.

more practical electrodes with high surface curvature (e.g., Si nanoparticle or nanowires) than the one in our model planar system. Nevertheless, the existing strain creates enough stress to cause rupture of the planar film. Therefore, even higher probability of SEI rupture is expected on convex electrodes. In contrast to convex surfaces, the concave surfaces would compress the SEI rather than stretch it. Consequently, the electrode volume expansion stress would be compensated by a radial compression, like in the case of Si-tubes covered with dielectric material. In this case, the knowledge of SEI Young's modulus and yield strength would allow calculation of the optimal electrode's curvature, i.e., the nanotube diameter.

For smooth films, such as the SEI after the first cycle, the thickness could be derived not only from the scratching test but also by indentation with a sharp nanoindenter. Because a S-AFM tip can penetrate an elastic film, the distance between the contact point and the hard-wall repulsion part of the force−indentation curve carries this information (Figure 6A). The SEI thickness was determined to be 23 to 24 nm. Thus, the indentation depth (typically 10−20% of the ultrathin film thickness) should be 2.5−5.0 nm, which exceeds the roughness (1.9 nm) and thus allows for the determination of the Young's modulus. In addition, the thickness of the film after the first cycle is comparable to that obtained after 10 cycles (25−30 nm). It appears that the thickness of the intrinsic SEI does not grow substantially upon cycling, though polymeric formations emerge on the surface, which originate from permanent stress and periodical rupture and renewal. This interpretation is consistent with earlier statements claiming that SEI grows mainly during the initial formation cathodic scan.[10,11,35]

Nanoindentation measurements were conducted with sharp AFM tips and spherical colloidal probes (CPs) on the SEI formed after the first (de)insertion cycle. Appropriate cantilever stiffness selection was achieved by using initial testing with cantilevers of various spring constants to fulfill the common sensitivity criteria.[21] For both nanoindenter geometries, the

DOI: 10.1021/acsami.5b06700
ACS Appl. Mater. Interfaces 2015, 7, 23554−23563

nanoindentation limit was set to 10 nN, though this value was beyond the limit of elastic film deformation. While the film was locally irreversibly deformed, a statistically significant amount of data was acquired by force-volume mapping of 8 × 8 points over a 40 × 40 μm^2 area, which ensures the absence of cross-deformation of the SEI between indentation points. Figure 6A shows typical force−indentation curves obtained upon loading with the S-AFM tip together with a fit to the Bilodeau approximation for a four-sided pyramid. The fit converges to the experimental data only within the initial 6 nm of indentation depth. We attribute this part of the curve to the elastic response of the SEI. Further increase of the loading force leads to plastic deformation of the SEI, which terminates when the tip penetrates the film completely. The silicon can be considered a hard wall because the cantilever stiffness (0.19 N/m) is much lower than the stiffness of the sample or tip material (both silicon).

The sigmoidal shape of the force−indentation curves (Figure 6A), which is typical for sharp indenter data,[7] was attributed to the specific stress response of ductile composite material, not as an evidence of two SEI sublayers. If the latter were the case, then a transition from "soft" response to "hard" response would be expected. However, the experiment revealed the opposite case, which is more typical for a rubber-like polymer or a composite material.[21] As demonstrated by Ruffo et al., the composite material (SEI) in 1 M $LiPF_6$ in EC:DEC (1:1 w/w) consists of PEO olygomers, hydrocarbons, and low molecular weight lithium salts.[34] Therefore, a polymer matrix filled with solvated low molecular weight salts can probably be regarded as a model, which describes the stress−strain (force−indentation) response of the SEI. On the basis of this, the preferential atomic content of carbon in the outer layer, revealed by Ruffo et al.[34] using XPS, can now be attributed to the polymeric formations emerged on the SEI surface.

Figure 6B shows a typical force−indentation curve obtained upon loading with a spherical CP, together with a fit to the Hertz model for a parabolic indenter. For this study, we used a CP with an intrinsic surface roughness below rms of ca. 2.1 nm (estimated over 1 × 1 μm^2), which is comparable to the rms roughness of the SEI (1.9 nm, 1 × 1 μm^2), but lower than the indentation depth over which an elastic response has been observed (5 to 7 nm). It should be noted that a fair fit to the model is observed at a low indentation depth, which is further supported by the plot of the force to the power of 2/3 as a function of the indentation depth (inset of Figure 6B). In this representation, the fit and the experimental curve appear linear and converge well. Similar evidence is provided for the convergence of the S-AFM tip indentation curve (inset Figure 6A) to the model, in which a square root of force is used to demonstrate linearity.

While the S-AFM indentation data is prone to local instabilities and film morphology variations, the CP data reflect an average response of a much larger area. As explained in the Theoretical Basis section, the S-AFM tips and spherical CPs complement each other in the determination of ultrathin film elasticity. First, the Young's modulus of the SEI as estimated from the tip data tends to overestimate the elasticity due to nonideal tip geometry and Bilodeau model shortages. The resulting histogram (Figure 6C) suggests that the most probable range of values is 2−20 MPa, although it should be noted that 60% of the values in this range are below 10 MPa. Second, the CP data tend to underestimate the elasticity because of averaging over surface gaps filled with solution, which are inevitably present on the rough surface. Figure 6D shows the representative results for the probability of SEI Young's modulus distribution as determined by indentation with CP. A peak value of ca. 0.5 MPa is determined from the inset of Figure 6D.

On the basis of cumulative data from both S-AFM tip and CP measurements, we estimate the effective Young's modulus of the SEI in liquid to be 0.5 to 10 MPa. This stiffness lies between hard gels and typical polyisoprene rubber.[21] Provided that the composite structure of SEI can be represented by a polymer matrix (phase 2, low E) and inorganic spherical particles (solvated salt crystals, phase 1, high E), the resulting elasticity seems to be determined to a large extent by the Young's modulus of the polymer matrix. A similar suggestion can be made based on the Takayanagi formula, representing the total elasticity as[36]

$$E = \left(\frac{\varphi}{E_1} + \frac{1 - \varphi}{E_2} \right)^{-1} \tag{4}$$

where E_1 and E_2 are Young's moduli of phases 1 and 2, and correspondingly, φ is the volume fraction of phase 1. Accordingly, since in the system $E_1 \gg E_2$ by default and the volume fraction of phase 2 is comparable to phase 1 within 1 order of magnitude, the resulting elasticity is determined mainly by the Young's modulus of the polymer matrix. This is an important consideration, because it opens a new aspect of designing artificial SEI films, for which various polymer layer architectures would be more favorable than stiff inorganic ones.[37]

Several groups have used an AFM-nanoindentation approach in order to determine the Young's modulus of the SEI on various electrodes.[7−11] Zhang et al. employed a sharp AFM tip to indent a dried SEI on MnO electrodes.[7] After the first lithiation−delithiation cycle, they reported a Young's modulus in the range between 1 MPa and 10 GPa, whereas the apparent thickness of the SEI layer, determined by indentation, varied from 10 to 150 nm. Similar values with large scattering were also found at different states of charge.[7] Ex situ indentation of dried SEI on silicon electrodes was conducted by Weadock et al.[8] and Xu et al.[9] using a CP and an S-AFM tip, respectively. The reported elasticity scattered in a large interval of 50 to 500 MPa in both cases, which is attributed to the large roughness factor of the SEI and local inhomogeneity of the film. Bearing in mind that the properties of the SEI may differ from those reported in literature due to a number of reasons (reactivity of the electrode material, composition of electrolyte solution, operating voltage, charging rate, temperature, etc.), three conclusions can still be derived by comparing the reported values to ours. (I) The roughness factor of the SEI and local inhomogeneity of the film must be seriously considered. (II) The wetness of the film can strongly affect the estimated values due to shrinkage and hardening upon drying of a polymer film, which contains solvated salts.[38,39] In the presence of solvent molecules, the so-called plastification effect causes the reduction of effective elasticity. (III) The presence of dried polymeric formations on the surface of SEI should also be taken into account since they can contribute to the scattering of data on elasticity and film thickness.

The determination of Young's modulus in liquid was only reported by Deng et al. and Liu et al. up to now.[10,11] Using highly oriented pyrolytic graphite (HOPG) as a model system and sharp AFM tip indentation, Deng et al. showed that the SEI

DOI: 10.1021/acsami.5b06700
ACS Appl. Mater. Interfaces 2015, 7, 23554−23563

formed in 1 M LiTFSI in EC:DEC has a Young's modulus of 45 ± 22 MPa.[10] This value is in the same order of magnitude as the one reported in this study, indicating a similar nature of the SEI on HOPG and on the Si electrode. Nevertheless, there are considerable differences in the SEI formation process of the two mentioned systems. Indeed, the reported SEI thickness on HOPG after one lithiation−delithiation cycle is twice as low as that on silicon (10.4 ± 0.2 nm vs 23−24 nm, respectively). The differences in SEI thickness between Si and graphite electrodes are consistent with the literature,[2] indicating that the passivating character of the SEI formed on HOPG appears to be more effective in protecting the electrode due to the differences in the kinetics of SEI formation. In situ investigation of morphological and mechanical changes of lithiated−delithiated Si nanowires was conducted by Liu et al. using S-AMF.[11] They estimated a Young's modulus at 50−400 MPa and reported a thickness of 28 ± 10 nm after the first cycle. Moreover, the highly adaptive nature of Si nanowires able to resist large volumetric changes (up to 200%, 1.5−0.01 V vs Li/Li^+) has been demonstrated.

5. CONCLUSIONS

Even a moderate cathodic cutoff potential of 0.1 V did not prevent the rupture and subsequent roughening of the SEI formed on Si electrodes due to volume changes upon cycling. Therefore, reliable values of the Young's modulus could only be estimated after the first cycle, when a relatively smooth surface (rms roughness of 2 nm) for a thickness of ca. 25 nm was obtained.

After multiple cycles, using force−volume mapping by means of spherical colloidal probes, polymeric formations (extended up to 300 nm into bulk solution) were detected on the surface of the SEI, whereas the intrinsic thickness of the SEI appeared to remain around 25 to 30 nm. The soft mechanical response and poor attachment to the probe make polymeric formations difficult to detect by AFM imaging methods.

The AFM-nanoindentation was carried out in working solution to keep the SEI wet and avoid the shrinkage and hardening of dried SEI films. Besides the ratio of roughness−indentation depth and the wetness of the film, the nanoindenter geometry was additionally considered in the determination of the Young's modulus. The Young's modulus was estimated using two nanoindenter types: a pyramidal AFM tip and spherical colloidal probes. The former tend to overestimate the value, while the latter underestimates it. Therefore, the actual Young's modulus is expected to lie between the values obtained with the two types of nanoindenters. We estimate the Young's modulus of the SEI on a Si electrode to be in the range of 0.5−10 MPa under the investigated conditions

AUTHOR INFORMATION

Corresponding Authors

*E-mail: wolfgang.schuhmann@rub.de. Tel: +49 234 32 26200.
*E-mail: edgar.ventosa@rub.de. Tel: +49 234 32 25586.

Notes

The authors declare no competing financial interest.

REFERENCES

(1) Wagner, F. T.; Lakshmanan, B.; Mathias, M. F. Electrochemistry and the Future of the Automobile. *J. Phys. Chem. Lett.* **2010**, *1*, 2204−2219.

(2) Obrovac, M. N.; Chevrier, V. L. Alloy Negative Electrodes for Li-Ion Batteries. *Chem. Rev.* **2014**, *114*, 11444−11502.

(3) Park, C.-M.; Kim, J.-H.; Kim, H.; Sohn, H.-J. Li-Alloy Based Anode Materials for Li Secondary Batteries. *Chem. Soc. Rev.* **2010**, *39*, 3115−3141.

(4) Jeong, S. K.; Inaba, M.; Mogi, R.; Iriyama, Y.; Abe, T.; Ogumi, Z. Surface Film Formation on a Graphite Negative Electrode in Lithium-Ion Batteries: Atomic Force Microscopy Study on the Effects of Film-Forming Additives in Propylene Carbonate Solutions. *Langmuir* **2001**, *17*, 8281−8286.

(5) Campana, F. P.; Kötz, R.; Vetter, J.; Novák, P.; Siegenthaler, H. In Situ Atomic Force Microscopy Study of Dimensional Changes During Li-Ion Intercalation/De-intercalation in Highly Oriented Pyrolytic Graphite. *Electrochem. Commun.* **2005**, *7*, 107−112.

(6) Alliata, D. Electrochemical SPM Investigation of the Solid Electrolyte Interphase Film Formed on HOPG Electrodes. *Electrochem. Commun.* **2000**, *2*, 436−440.

(7) Zhang, J.; Wang, R.; Yang, X.; Lu, W.; Wu, X.; Wang, X.; Li, H.; Chen, L. Direct Observation of Inhomogeneous Solid Electrolyte Interphase on MnO Anode with Atomic Force Microscopy and Spectroscopy. *Nano Lett.* **2012**, *12*, 2153−2157.

(8) Weadock, N.; Varongchayakul, N.; Wan, J.; Lee, S.; Seog, J.; Hu, L. Determination of Mechanical Properties of the SEI in Sodium Ion Batteries via Colloidal Probe Microscopy. *Nano Energy* **2013**, *2*, 713−719.

(9) Xu, W.; Vegunta, S. S. S.; Flake, J. C. Surface-Modified Silicon Nanowire Anodes for Lithium-ion Batteries. *J. Power Sources* **2011**, *196*, 8583−8589.

(10) Deng, X.; Liu, X.; Yan, H.; Wang, D.; Wan, L. Morphology and Modulus Evolution of Graphite Anode in Lithium Ion Battery: An in situ AFM Investigation. *Sci. China: Chem.* **2014**, *57*, 178−183.

(11) Liu, X.; Deng, X.; Liu, R.; Yan, H.; Guo, Y.; Wang, D.; Wan, L. Single Nanowire Electrode Electrochemistry of Silicon Anode by in Situ Atomic Force Microscopy: Solid Electrolyte Interphase Growth and Mechanical Properties. *ACS Appl. Mater. Interfaces* **2014**, *6*, 20317−20323.

(12) Li, H.; Vlassak, J. J. Determining the Elastic Modulus and Hardness of an Ultra-Thin Film on a Substrate Using Nano-indentation. *J. Mater. Res.* **2009**, *24*, 1114−1126.

(13) Butt, H.-J.; Cappella, B.; Kappl, M. Force Measurements with the Atomic Force Microscope: Technique, Interpretation and Applications. *Surf. Sci. Rep.* **2005**, *59*, 1−152.

(14) Kasavajjula, U.; Wang, C.; Appleby, A. J. Nano- and Bulk-Silicon-Based Insertion Anodes for Lithium-ion Secondary Cells. *J. Power Sources* **2007**, *163*, 1003−1039.

(15) Maranchi, J. P.; Hepp, A. F.; Kumta, P. N. High Capacity, Reversible Silicon Thin-Film Anodes for Lithium-Ion Batteries. *Electrochem. Solid-State Lett.* **2003**, *6*, A198.

(16) Zinn, A.-H.; Wieczorek, N.; Borhani-Haghighi, S.; Schuhmann, W.; Ventosa, E.; Ludwig, A. Indentation of Lithiated and Delithiated Si Anodes. *Phys. Status Solidi A* **2014**, *211*, 2650−2650.

(17) Zampardi, G.; Ventosa, E.; La Mantia, F.; Schuhmann, W. In situ Visualization of Li-ion Intercalation and Formation of the Solid Electrolyte Interphase on TiO2-Based Paste Electrodes Using Scanning Electrochemical Microscopy. *Chem. Commun.* **2013**, *49*, 9347−9349.

(18) Kuznetsov, V.; Papastavrou, G. Note: Mechanically and Chemically Stable Colloidal Probes from Silica Particles for Atomic Force microscopy. *Rev. Sci. Instrum.* **2012**, *83*, 116103.

(19) Hutter, J. L.; Bechhoefer, J. Calibration of Atomic-Force Microscope Tips. *Rev. Sci. Instrum.* **1993**, *64*, 1868−1873.

(20) Mogharebi, R.; Kazakeviciute-Makovska, R.; Steeb, H.; Eggeler, G.; Neuking, S.; Neuking, K. On the Cyclic Material Stability of Shape Memory Polymer. *Materialwiss. Werkstofftech.* **2013**, *44*, 521−526.

(21) Tsukruk, V. V.; Gorbunov, V. V.; Huang, Z.; Chizhik, S. A. Dynamic Microprobing of Viscoelastic Polymer Properties. *Polym. Int.* **2000**, *49*, 441−444.

(22) Chizhik, S. A.; Huang, Z.; Gorbunov, V. V.; Myshkin, N. K.; Tsukruk, V. V. Micromechanical Properties of Elastic Polymeric Materials As Probed by Scanning Force Microscopy. *Langmuir* **1998**, *14*, 2606−2609.

DOI: 10.1021/acsami.5b06700
ACS Appl. Mater. Interfaces 2015, 7, 23554−23563

(23) Lin, D. C.; Dimitriadis, E. K.; Horkay, F. Elasticity Models for the Spherical Indentation of Gels and Soft Biological Tissues. *MRS Online Proc. Libr.* **2007**, *1060*, 1060-LL05−07.
(24) Greaves, G. N.; Greer, A. L.; Lakes, R. S.; Rouxel, T. Poisson's Ratio and Modern Materials. *Nat. Mater.* **2011**, *10*, 823−837.
(25) Bilodeau, G. G. Regular Pyramid Punch Problem. *J. Appl. Mech.* **1992**, *59*, 519.
(26) Graetz, J.; Ahn, C. C.; Yazami, R.; Fultz, B. Highly Reversible Lithium Storage in Nanostructured Silicon. *Electrochem. Solid-State Lett.* **2003**, *6*, A194−A197.
(27) Baranchugov, V.; Markevich, E.; Pollak, E.; Salitra, G.; Aurbach, D. Amorphous Silicon Thin Films as a High Capacity Anodes for Li-ion Batteries in Ionic Liquid Electrolytes. *Electrochem. Commun.* **2007**, *9*, 796−800.
(28) Choi, N.-S.; Yao, Y.; Cui, Y.; Cho, J. One Dimensional Si/Sn - Based Nanowires and Nanotubes for Lithium-Ion Energy Storage Materials. *J. Mater. Chem.* **2011**, *21*, 9825−9840.
(29) Chan, C. K.; Chan, a. K.; Ruffo, R.; Hong, S. S.; Huggins, R. A.; Cui, Y. Structural and Electrochemical Study of the Reaction of Lithium with Silicon Nanowires. *J. Power Sources* **2009**, *189*, 34−39.
(30) Lucas, I. T.; Pollak, E.; Kostecki, R. In situ AFM Studies of SEI Formation at a Sn Electrode. *Electrochem. Commun.* **2009**, *11*, 2157−2160.
(31) Israelachvili, J. N. *Intermolecular and Surface Forces*; Academic Press: Burlington, MA, 2011; pp 381−413.
(32) Oumellal, Y.; Delpuech, N.; Mazouzi, D.; Dupre, N.; Gaubicher, J.; Moreau, P.; Soudan, P.; Lestriez, B.; Guyomard, D. The Failure Mechanism of Nano-Sized Si-Based Negative Electrodes for Lithium Ion Batteries. *J. Mater. Chem.* **2011**, *21*, 6201−6208.
(33) Pereira-Nabais, C.; Światowska, J.; Chagnes, A.; Ozanam, F.; Gohier, A.; Tran-Van, P.; Cojocaru, C.-S.; Cassir, M.; Marcus, P. Interphase Chemistry of Si Electrodes Used as Anodes in Li-ion Batteries. *Appl. Surf. Sci.* **2013**, *266*, 5−16.
(34) Ruffo, R.; Hong, S. S.; Chan, C. K.; Huggins, R. A.; Cui, Y. Impedance Analysis of Silicon Nanowire Lithium Ion Battery Anodes. *J. Phys. Chem. C* **2009**, *113*, 11390−11398.
(35) Tokranov, A.; Sheldon, B. W.; Li, C.; Minne, S.; Xiao, X. In Situ Atomic Force Microscopy Study of Initial Solid Electrolyte Interphase Formation on Silicon Electrodes for Li-Ion Batteries. *ACS Appl. Mater. Interfaces* **2014**, *6*, 6672−6686.
(36) Schlicke, H.; Leib, E. W.; Petrov, A.; Schröder, J. H.; Vossmeyer, T. Elastic and Viscoelastic Properties of Cross-Linked Gold Nanoparticles Probed by AFM Bulge Tests. *J. Phys. Chem. C* **2014**, *118*, 4386−4395.
(37) Menkin, S.; Golodnitsky, D.; Peled, E. Artificial Solid-Electrolyte Interphase (SEI) for Improved Cycleability and Safety of Lithium-ion Cells for EV Applications. *Electrochem. Commun.* **2009**, *11*, 1789−1791.
(38) Lisunova, M. O.; Drachuk, I.; Shchepelina, O. A.; Anderson, K. D.; Tsukruk, V. V. Direct Probing of Micromechanical Properties of Hydrogen-Bonded Layer-by-Layer Microcapsule Shells with Different Chemical Compositions. *Langmuir* **2011**, *27*, 11157−11165.
(39) Trenkenschuh, K.; Erath, J.; Kuznetsov, V.; Gensel, J.; Boulmedais, F.; Schaaf, P.; Papastavrou, G.; Fery, A. Tuning of the Elastic Modulus of Polyelectrolyte Multilayer Films built up from Polyanions Mixture. *Macromolecules* **2011**, *44*, 8954−8961.

DOI: 10.1021/acsami.5b06700
ACS Appl. Mater. Interfaces 2015, 7, 23554−23563